

Andromeda stream, a number of follow-up observational programmes are required, including an extension of the panoramic survey not only to the northern regions of the halo of M31, but also out to larger radii, as it is evident in the present data that the stream extends beyond the 40-kpc limits of the survey. The proximity of M31 also provides us with an opportunity to undertake a spectroscopic survey of individual stars within the stream, allowing us to map its kinematic and chemical properties. As with the tidal material detected in the halo of our own Galaxy, studies of the Andromeda stream would allow us to map the distribution of dark matter within the halo of our nearest neighbouring galaxy, as well as furthering our understanding of the process of galaxy formation. □

Received 9 February; accepted 4 May 2001.

1. Putman, M. E. *et al.* Tidal disruption of the Magellanic Clouds by the Milky Way. *Nature* **394**, 752–754 (1998).
2. Ibata, R., Lewis, G. F., Irwin, M., Totten, E. & Quinn, T. Great circle tidal streams: evidence for a nearly spherical massive dark halo around the Milky Way. *Astrophys. J.* **551**, 294–311 (2001).
3. Ibata, R., Irwin, M., Lewis, G. F. & Stolte, A. Galactic halo substructure in the Sloan Digital Sky Survey: The ancient tidal stream from the Sagittarius dwarf galaxy. *Astrophys. J.* **547**, L133–L136 (2001).
4. Helmi, A., White, S. D. M., de Zeeuw, P. T. & Zhao, H. Debris streams in the solar neighbourhood as relicts from the formation of the Milky Way. *Nature* **402**, 53–55 (1999).
5. Klyin, A., Gottlöber, S., Kravtsov, A. V. & Khokhlov, A. M. Galaxies in N-body simulations: Overcoming the overmerging problem. *Astrophys. J.* **516**, 530–551 (1999).
6. Cole, S., Aragon-Salamanca, A., Frenk, C. S., Navarro, J. F. & Zepf, S. E. A recipe for galaxy formation. *Mon. Not. R. Astron. Soc.* **271**, 781–806 (1994).
7. Eggen, O. J., Lynden-Bell, D. & Sandage, A. R. Evidence from the motions of old stars that the Galaxy collapsed. *Astrophys. J.* **136**, 748–766 (1962).
8. Shang, Z. *et al.* Ring structure and warp of NGC 5907: Interaction with dwarf galaxies. *Astrophys. J.* **504**, L23–L26 (1998).
9. Sackett, P. D., Morrison, H. L., Harding, P. & Boroson, T. A. A faint luminous halo that may trace the dark matter around spiral galaxy NGC 5907. *Nature* **370**, 441–443 (1994).
10. Stanek, K. Z. & Garnavich, P. M. Distance to M31 with the Hubble Space Telescope and HIPPARCOS red clump stars. *Astrophys. J.* **503**, L131–L134 (1998).
11. Irwin, M. & Lewis, J. INT WFS pipeline processing. *New Astron. Rev.* **45**, 105–110 (2001).
12. Holland, S., Fahlan, G. G. & Richer, H. B. Deep HST V- and I-band observations of the halo of M31: Evidence for multiple stellar populations. *Astron. J.* **112**, 1035–1045 (1996).
13. Rich, R. M., Mighell, K. J., Freedman, W. L. & Neill, J. D. Local Group populations with the Hubble Space Telescope. I. The M31 globular cluster G1=Mayall II. *Astron. J.* **111**, 768–776 (1996).
14. Reitzel, D. B., Guhathakurta, P. & Gould, A. Isolating red giant stars in M31's elusive outer spheroid. *Astron. J.* **116**, 707–722 (1998).
15. Walterbos, R. A. M. & Kennicutt, R. C. Multi-color photographic surface photometry of the Andromeda galaxy. *Astron. Astrophys. Suppl.* **69**, 311–332 (1987).
16. Innanen, K. A., Kamper, K. W., van den Bergh, S. & Papp, K. A. The optical warp of M31. *Astrophys. J.* **254**, 515–516 (1982).
17. Durrell, P. R., Harris, W. E., Pritchett, C. J. & Davidge, T. Photometry of the outer halo of M31. *Am. Astron. Soc. Meeting* **195**, 4.04 (1999).
18. Ferguson, A. M. N., Gallagher, J. S. & Wyse, R. F. G. The extreme outer regions of disk galaxies. I. Chemical abundances of H II regions. *Astron. J.* **116**, 673–690 (1998).
19. Lee, M. G. Stellar population is the central region of the dwarf elliptical galaxy NGC 205. *Astron. J.* **112**, 1438–1449 (1996).
20. Young, L. M. & Lo, K. Y. The neutral interstellar medium in nearby dwarf galaxies. II. NGC 185, NGC 205, and NGC 147. *Astrophys. J.* **476**, 127–143 (1997).
21. Hodge, P. W. The structure and content of NGC 205. *Astrophys. J.* **182**, 671–696 (1973).
22. Bender, R., Paquet, A. & Nieto, J. Internal stellar kinematics of three dwarf ellipticals in the Local Group. *Astron. Astrophys.* **246**, 349–353 (1991).
23. Welch, G. A., Sage, L. J. & Mitchell, G. F. The puzzling features of the interstellar medium in NGC 205. *Astrophys. J.* **499**, 209–220 (1998).
24. Freedman, W. L. Stellar content of nearby galaxies. II—the Local Group dwarf elliptical galaxy M32. *Astron. J.* **98**, 1285–1304 (1989).
25. Davidge, T. J. The evolved red stellar content of M32. *Publ. Astron. Soc. Pacif.* **112**, 1177–1187 (2000).
26. Grillmair, C. J. *et al.* Hubble Space Telescope observations of M32: The color-magnitude diagram. *Astron. J.* **112**, 1975–1987 (1996).
27. Johnston, K. V., Spergel, D. N. & Hernquist, L. The disruption of the Sagittarius dwarf galaxy. *Astrophys. J.* **451**, 598–606 (1995).
28. Ibata, R. A. & Lewis, G. F. Galactic indigestion: Numerical simulations of the Milky Way's closest neighbor. *Astrophys. J.* **500**, 575–590 (1998).
29. Schwarzschild, M. Mass distribution and mass-luminosity ratio in galaxies. *Astron. J.* **59**, 273–284 (1954).
30. Ibata, R. A. & Razoumov, A. O. Archer of the Galactic disk? The effect on the outer HI disk of the Milky Way of collisional encounters with the Sagittarius dwarf galaxy. *Astron. Astrophys.* **336**, 130–136 (1998).

Acknowledgements

This paper is based on observations made with the Isaac Newton Telescope operated on the island of La Palma by the Isaac Newton Group in the Spanish Observatorio del Roque de los Muchachos of the Instituto de Astrofísica de Canarias.

Correspondence and requests for materials should be addressed to R.I. (e-mail: ibata@astro.u-strasbg.fr).

Dynamical tunnelling of ultracold atoms

W. K. Hensinger*†, H. Häffner*, A. Browaeys*, N. R. Heckenberg†, K. Helmerson*, C. McKenzie*, G. J. Milburn‡, W. D. Phillips*, S. L. Rolston*, H. Rubinsztein-Dunlop† & B. Upcroft†‡

* National Institute of Standards and Technology, Gaithersburg, Maryland 20899, USA

† Centre for Laser Science, Department of Physics, ‡ Centre for Quantum Computer Technology, The University of Queensland, Brisbane, Queensland 4072, Australia

The divergence of quantum and classical descriptions of particle motion is clearly apparent in quantum tunnelling^{1,2} between two regions of classically stable motion. An archetype of such non-classical motion is tunnelling through an energy barrier. In the 1980s, a new process, ‘dynamical’ tunnelling^{1–3}, was predicted, involving no potential energy barrier; however, a constant of the motion (other than energy) still forbids classically the quantum-allowed motion. This process should occur, for example, in periodically driven, nonlinear hamiltonian systems with one degree of freedom^{4–6}. Such systems may be chaotic, consisting of regions in phase space of stable, regular motion embedded in a sea of chaos. Previous studies predicted⁴ dynamical tunnelling between these stable regions. Here we observe dynamical tunnelling of ultracold atoms from a Bose–Einstein condensate in an amplitude-modulated optical standing wave. Atoms coherently tunnel back and forth between their initial state of oscillatory motion (corresponding to an island of regular motion) and the state oscillating 180° out of phase with the initial state.

Tunnelling between discrete states is coherent and reversible—that is, the particle oscillates between the states, which is the process we describe here. Coherent tunnelling oscillations are especially significant, as the system must pass through states corresponding to superpositions of distinct classical motions. It has been suggested⁷ that such states are strongly suppressed by decoherence, a subject of central importance to quantum information. Our system should

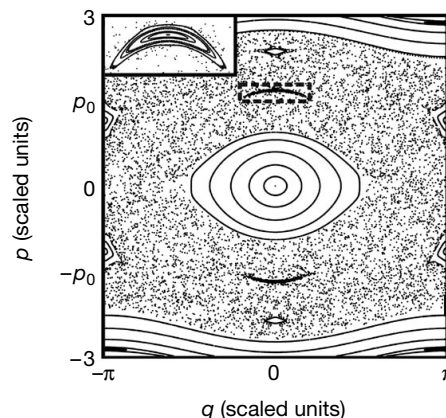


Figure 1 Poincaré section for position p and momentum q of a classical particle in an amplitude-modulated optical lattice. Data are shown for $\kappa = 1.66$ and $\epsilon = 0.29$, showing a mixed phase space. The central region consists of small-amplitude stable motion. Chaos separates this region from two period-one resonances located above and below the centre along $q = 0$. Further out in momentum are two stable regions of motion known as librations, which have a period of twice the modulation period. At the edges are bands of regular motion corresponding to above-barrier motion. The inset is a magnified view of the dashed rectangle.

provide a test of this suggestion in the context of tunnelling in a nonlinear dynamical system.

Atoms in optical potentials^{8–11} provide an ideal test bed to explore quantum nonlinear dynamics. The quantum driven pendulum, a paradigmatic system for the study of ‘quantum chaos’, is realized by a periodically modulated optical standing wave, which can provide a highly non-dissipative, one-dimensional potential. Using ultracold trapped atoms whose action is of the order of Planck’s constant makes quantum effects significant. Atoms in a standing wave, detuned far from an atomic resonance, with sinusoidal amplitude modulation, are described by the centre-of-mass hamiltonian:

$$H(t) = \frac{p^2}{2} + 2\kappa(1 + 2\epsilon \sin\omega t) \sin^2(q/2)$$

where $q = 2kx$ and $p = (2k/m\omega)p_x$ are the scaled position and momentum variables respectively, t is the time, $\kappa = 4U_0^2\omega_R/\omega^2$ is the scaled well depth, ω is the modulation frequency, $\omega_R = \hbar k^2/2m$ is the atomic recoil frequency, U_0 is the well depth in units of $\hbar\omega_R$, and ϵ is the modulation parameter. The position and momentum along the standing wave are x and p_x , m is the mass, $k = 2\pi/\lambda$ is the wavevector, and λ is the wavelength of the optical standing wave. The classical system described by this hamiltonian has a mixed phase space having regions of regular motion embedded in a sea of chaos. The Poincaré section shown in Fig. 1 displays stroboscopically the atomic position and momentum at time intervals equal to the modulation period. The Poincaré section is plotted for experimental parameters $\kappa = 1.66$ and $\epsilon = 0.29$. Islands of regular motion (boomerang-shaped rings—see Fig. 1 inset) surround period-one resonances (fixed points) where the atomic motion remains exactly in phase with the modulation (a period-one resonance rotates 360° around the origin in one modulation period).

Figure 2 shows a graphical representation of these period-one resonances. For small changes in κ and ϵ (within our experimental uncertainties), the period-one regions of regular motion can split into two closely spaced period-two regions. For initial conditions reflecting the Heisenberg uncertainty limit in our experiment, such behaviour would be indistinguishable from period-one motion. The chaotic sea of Fig. 1 (dotted region) is bounded in momentum by the region of regular unbound motion, where atoms have enough energy to move along from one well to the next. The ellipses in Fig. 1 represent Kolmogorov–Arnold–Moser (KAM) surfaces¹², the crossing of which is forbidden by classical mechanics. A detailed experimental and theoretical study of the dynamics of the driven pendulum using cold atoms may be found in previous publications^{10,11}.

The quantum dynamics of a periodically driven hamiltonian system can be described in terms of the eigenstates of the Floquet operator F , which evolves the system in time by one modulation period. The Floquet eigenstates can be associated with regions of regular and irregular motion of the classical map⁴. The localized

Floquet eigenstates do not necessarily overlap well with the regions of regular motion of the classical Poincaré map, except in the semiclassical limit of large action. Initial states localized in the stable region around a fixed point in the Poincaré section can be associated with superpositions of a small number of Floquet eigenstates. For an appropriate choice of parameters the phase space exhibits two period-one fixed points, which for a suitable Poincaré section lie on the momentum axis at $\pm p_0$, as in Fig. 1. For certain values of κ and ϵ there are two dominant Floquet states $|\phi_\pm\rangle$ that are localized on both fixed points but are distinguished by being even or odd eigenstates of the parity operator that changes the sign of momentum. A state localized on just one fixed point is therefore likely to have dominant support on an even or odd superposition of these two Floquet states: $|\psi(\pm p_0)\rangle \approx (|\phi_+\rangle \pm |\phi_-\rangle)/\sqrt{2}$. The evolution is described by repeated application of the Floquet operator. As this is a unitary operator, $F|\phi_\pm\rangle = e^{-i\phi_\pm}|\phi_\pm\rangle$. Thus at a time which is n times the period of modulation, the state initially localized on $+p_0$ evolves to $|\Psi(n)\rangle \approx (e^{-in\phi_+}|\phi_+\rangle + e^{-in\phi_-}|\phi_-\rangle)/\sqrt{2}$. Ignoring an overall phase and defining the separation between Floquet quasi-energies as $\Delta\phi = \phi_- - \phi_+$, we obtain $|\Psi(n)\rangle \approx (|\phi_+\rangle + e^{-in\Delta\phi}|\phi_-\rangle)/\sqrt{2}$. At $n = \pi/\Delta\phi$ periods, the state will form the anti-symmetric superposition of Floquet states and thus is localized on the other fixed point at $-p_0$. In other words, the system has tunneled from one of the fixed points to the other^{4,6}. This is reminiscent of barrier tunnelling between two wells, where a particle in one well, a superposition of symmetric and antisymmetric energy eigenstates, oscillates between wells with a frequency given by the energy difference between the eigenstates.

We prepared atoms in a superposition of Floquet states associated with one of the fixed points as follows. A Bose–Einstein condensate with approximately 3×10^6 sodium atoms was prepared¹³ in a magnetic trap with trapping frequencies $2\omega_x = \sqrt{2}\omega_y = \omega_z = 2\pi \times 33$ Hz, which, using a scattering length of 2.8 nm, results in calculated Thomas–Fermi diameters of 83, 57 and 42 μm , respectively. We release the condensate and adiabatically turn on a one-dimensional standing-wave lattice along z . The gaussian lattice beams are detuned ~ 14 GHz above the atomic D2 resonance ($\lambda = 589$ nm) and have a waist $w \approx 250$ μm , leading to an intensity variation of less than 5% across the atomic cloud. We determine κ from a one-dimensional band structure calculation using the measured oscillation frequency of atoms in the unmodulated standing wave. Its 10% uncertainty is due to uncertainty in measuring the oscillation frequency and to variations in the laser intensity (all reported uncertainties are 1 s.d. combined systematic and statistical uncertainties).

The atoms are loaded into the bottom of the lowest band (quasimomentum equal to 0) of the optical lattice (we have verified that $> 99\%$ of the atomic population is in the lowest band). Each individual well contains a minimum uncertainty wave packet with an r.m.s. spread of 0.6 in scaled units. To load selectively only the region around one resonance, we suddenly shift the position of the standing wave by inducing an appropriate phase shift with an

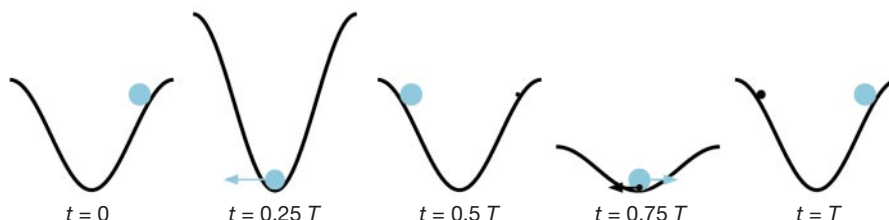


Figure 2 Diagram of period-one resonances of an atom in an amplitude-modulated sinusoidal potential. These resonances correspond to atomic motion that remains in phase with the modulation frequency. The anharmonicity of the sinusoidal potential is compensated by the amplitude modulation for atoms around these resonances, creating

the regions of regular period-one motion shown in Fig. 1. The appearance of the second ball at $0.5T$ depicts tunnelling into the initially empty resonance. T is the modulation period, and t is time.

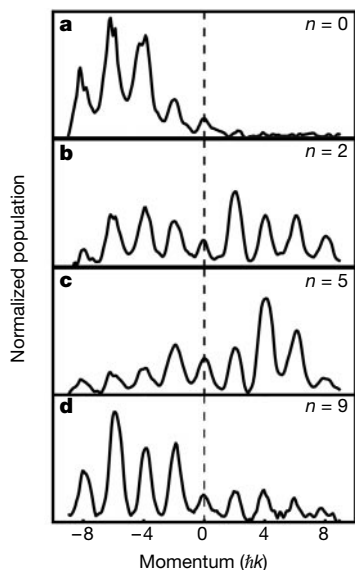


Figure 3 Atomic momentum distributions after n modulation periods, showing dynamical tunnelling. The parameters for this experiment were $\kappa = 1.66$, $\epsilon = 0.29$ and $\omega/2\pi = 250$ kHz.

acousto-optical modulator. Shortly (100–300 ns) before the phase shift, we start (at $t = 0$) to modulate the standing wave at $\omega/2\pi = 220$ – 320 kHz. The modulation frequency was chosen to optimize both the overlap between the wave packet and the region of regular motion, and to make the typical action of a particle¹⁰ small enough to observe quantum effects. After the atoms have interacted with the modulated standing wave for a selected number of modulation periods, the standing wave is turned off with the modulation phase chosen so that the resonance lies on the momentum axis at that time. Classically at that phase ($n + 0.25$ or 0.75 periods) the atoms, contained inside the region of regular motion, are at the bottom of the well, moving with maximum momentum, $\pm p_0$ (see fig. 2). We measure the atomic momentum distribution with absorption imaging after 1.5 ms of free flight. The momentum distribution appears as a set of ‘diffraction’ peaks at integer multiples of $2\hbar k$ due to the atomic coherence over the multiple wells of the optical lattice¹³.

Figure 3 depicts atomic momentum distributions for different interaction times with the modulated standing wave. In Fig. 3a we show the distribution immediately after loading one resonance region. This distribution consists mainly of a pair of diffraction peaks at $4\hbar k$ and $6\hbar k$. Classically, the atoms should remain in the resonance so the stroboscopically measured momentum distribution is unchanged. To the contrary, in Fig. 3b about half of the atoms have appeared with opposite momenta, which correspond to the other resonance region. Most of the atoms are found there by 5.25 modulation periods (Fig. 3c). At 9.25 modulation periods the atoms have returned to the original resonance as shown in Fig. 3d. This transfer of atoms back and forth between the regions of regular motion is coherent dynamical tunnelling.

In Fig. 4a we plot the mean atomic momentum after multiples of the modulation period. The blue (red) data points correspond to turning off the standing wave at the maximum (minimum) of the amplitude modulation (see Fig. 2 at $t = 0.25 T$ and $t = 0.75 T$). We observe an oscillation of the mean momentum indicating the occurrence of dynamical tunnelling for each set of data points. The period-one character of the motion is verified by the reversal of the momentum between the blue and red curves in Fig. 4a, which are separated in time by 0.5 modulation periods. By Fourier-transforming our data, we find the tunnelling period to be

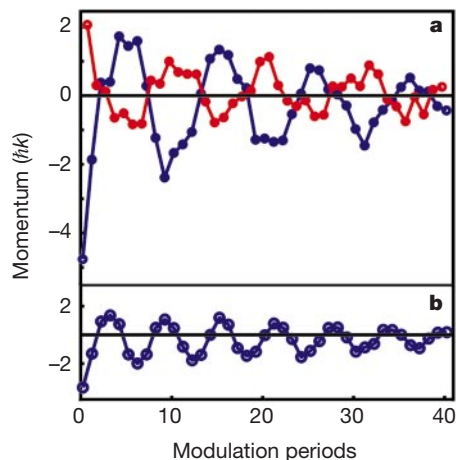


Figure 4 Mean momentum as a function of the number of modulation periods, n . **a**, The two curves correspond to two different ending phases ($n + 0.25$ (blue), $n + 0.75$ (red)) of the modulation (parameters as in Fig. 3). **b**, A slower decay of the tunnelling oscillations is seen for $\epsilon = 0.30$, $\kappa = 1.82$, and $\omega/2\pi = 222$ kHz.

10.3(2) modulation periods where the uncertainty is statistical. We performed a quantum simulation¹¹ for the system parameters of our experiment. The period of the tunnelling oscillation agrees with the experiment within the uncertainty (dominated by the uncertainty in κ); however, the envelope of the oscillations is different. Our simulations assume the presence of only 6 wells, whereas in the experiment about 150 are populated. The initial conditions of the calculations populated a single well (a superposition of all quasimomenta), and showed that the envelope of the oscillations depends sensitively on the number of wells. It is clear that coherence between wells (associated with quasimomentum = 0) must be included to accurately model our experiment. We note that the mean momenta of the blue and the red data points in Fig. 4a are slightly different for the same number of modulation periods. Classical theory predicts slightly different momenta of the fixed points when viewed at the phases corresponding to Fig. 2 at $t = 0.25 T$ and $t = 0.75 T$.

In Fig. 5 we display the atomic momentum distributions corresponding to the blue curve of Fig. 4a, as a function of the number of modulation periods. Because all atoms start on one side of the potential well, at 0.25 modulation periods essentially all atoms have negative momentum. By 1.25 periods the atoms that were loaded into the chaotic region have begun to spread out, forming a broad background, while the other atoms are bound inside the region of regular motion. For subsequent pictures the coherent oscillation between the two regions of regular motion is evident. We note that there is no significant (above-background) zero momentum peak even in the case of approximately zero mean momentum (when the atoms have tunnelled half way). This indicates that at half the tunnel period the system is in a coherent superposition of two distinguishable classical motions: one with positive momenta and one with equal but opposite momenta. We expect this, because quantum Floquet analysis shows that atoms tunnel from one region of regular motion into the other and it is impossible for them to enter the central island of stability at $(p, q) = (0, 0)$.

Classical simulations using a gaussian phase space distribution corresponding to our experimental wave packet (which is always bigger than the classical region of regular motion) show that for the conditions of Fig. 1 and for all experimental conditions, there is no behaviour similar to the observed oscillatory quantum tunnelling. The decay of the tunnelling oscillations may be due to a number of factors. One likely cause for the decay is spatial variations of κ , which lead to a dephasing of the tunnelling oscillations. Another possibil-

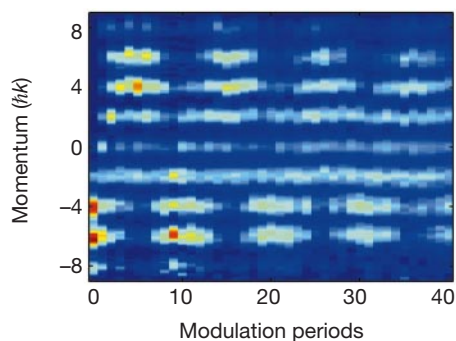


Figure 5 Momentum distributions as a function of the number of modulation periods, showing the tunnelling oscillation between negative and positive momenta. We note that the zero-momentum state remains mostly unpopulated, even when the mean momentum is zero. The colour coding ranges from blue to red for atomic populations ranging from small to large.

ity is that the tails of the oscillating quantum wave packets may extend outside the region of regular motion, allowing the atoms to ‘leak out’ into the classically chaotic region. This possibility is currently under investigation. The contribution of multiple Floquet states could lead to complicated multi-frequency oscillations, and an envelope for the tunnel oscillations appearing as decay, as observed for some parameters in our simulations. The effects of spontaneous emission and atom–atom interactions should be small.

Quantum theory predicts dynamical tunnelling to occur for various values of the scaled well depth κ , the modulation parameter ϵ and modulation frequency ω , and also predicts a strong sensitivity of the tunnelling period and amplitude on these parameters. For $\epsilon = 0.23$, $\kappa = 1.75$ and $\omega/2\pi = 250$ kHz we measured a tunnelling period of approximately 13 modulation periods. As shown in Fig. 4b, for $\epsilon = 0.30$, $\kappa = 1.82$ and $\omega/2\pi = 222$ kHz we find a tunnelling period of 6 modulation periods with a significantly longer decay time than in Fig. 4a. We have also experimentally observed an increase in the tunnelling period when κ is decreased and when all other parameters are held constant. This is the opposite of what one would expect for spatial barrier tunnelling.

Our observation of dynamical tunnelling of atoms in a modulated standing wave opens the door to further studies in quantum nonlinear dynamics. By varying the hamiltonian parameters and the initial conditions, we observe dynamical tunnelling for a variety of mixed phase space configurations. This may be ‘chaos-assisted tunnelling’, and a tunnelling rate that varies wildly as system parameters are changed would be a signature of such tunnelling¹. By introducing noise or spontaneous emission in a controlled manner, we could systematically investigate the role of decoherence in tunnelling and explore the classical limit of chaotic systems. By carefully following the evolution of wave packets loaded into the chaotic region from a Bose–Einstein condensate, we could probe ‘quantum chaos’ with the unprecedented resolution afforded by minimum uncertainty wave packets.

During the preparation of this Letter, we learned of an experiment¹⁴ reporting tunnelling of a different motional state in a similar system. □

Received 10 May; accepted 12 June 2001.

1. Tomsovic, S. Tunneling and chaos. *Physica Scripta T* **90**, 162–165 (2001).
2. Caldeira, A. O. & Leggett, A. J. Quantum tunneling in a dissipative system. *Ann. Phys.* **149**, 374–456 (1983).
3. Davis, M. J. & Heller, E. J. Quantum dynamical tunneling in bound states. *J. Chem Phys.* **75**, 246–254 (1981).
4. Dyrting, S., Milburn, G. J. & Holmes, C. A. Nonlinear quantum dynamics at a classical second order resonance. *Phys. Rev. E* **48**, 969–978 (1993).

5. Haake, F., Kus, M. & Scharf, R. Classical and quantum chaos for a kicked top. *Z. Phys. B* **65**, 381–395 (1987).
6. Sanders, B. C. & Milburn, G. J. The effect of measurement on the quantum features of a chaotic system. *Z. Phys. B* **77**, 497–510 (1989).
7. Habib, S., Shizume, K. & Zurek, W. H. Decoherence, chaos, and the correspondence principle. *Phys. Rev. Lett.* **80**, 4361–4365 (1998).
8. Graham, R., Schlautmann, M. & Zoller, P. Dynamical localization of atomic-beam deflection by a modulated standing light wave. *Phys. Rev. A* **45**, R19–R22 (1992).
9. Moore, F. L., Robinson, J. C., Bharucha, C. F., Sundaram, B. & Raizen, M. G. Atom optics realization of the quantum δ -kicked rotor. *Phys. Rev. Lett.* **75**, 4598–4601 (1995).
10. Hensinger, W. K., Truscott, A. G., Upcroft, B., Heckenberg, N. R. & Rubinsztein-Dunlop, H. Atoms in an amplitude-modulated standing wave—dynamics and pathways to quantum chaos. *J. Opt. B* **2**, 659–667 (2000).
11. Hensinger, W. K. *et al.* Experimental study of the quantum driven pendulum and its classical analog in atom optics. *Phys. Rev. A* (in the press).
12. Arnold, V. I. *Mathematical Methods of Classical Mechanics* (Springer, New York, 1979).
13. Kozuma, M. *et al.* Coherent splitting of Bose-Einstein condensed atoms with optically induced Bragg diffraction. *Phys. Rev. Lett.* **82**, 871–875 (1999).
14. Steck, D. A., Oskay, W. H. & Raizen, M. G. Observation of chaos-assisted tunneling between islands of stability. *Science* (in the press).

Acknowledgements

We thank C. Holmes for discussions. The NIST group was supported by the ONR, NASA and ARDA, and the University of Queensland group was supported by the ARC. A.B. was partially supported by DGA (France), and H. H. was partially supported by the A. v. Humboldt Foundation. W.K.H. and B.U. thank NIST for hospitality during the experiments.

Correspondence and requests for materials should be addressed to W.K.H. (e-mail: hensinge@physics.uq.edu.au).

Quantum interference of superfluid ³He

R. W. Simmonds, A. Marchenkov, E. Hoskinson, J. C. Davis & R. E. Packard

Physics Department, University of California, Berkeley, California 94720, USA

Celebrated interference experiments have demonstrated the wave nature of light¹ and electrons², quantum interference being the manifestation of wave–particle duality. More recently, double-path interference experiments have also demonstrated the quantum-wave nature of beams of neutrons³, atoms⁴ and Bose–Einstein condensates⁵. In condensed matter systems, double-path quantum interference is observed in the d.c. superconducting quantum interference device⁶ (d.c. SQUID). Here we report a double-path quantum interference experiment involving a liquid: superfluid ³He. Using a geometry analogous to the superconducting d.c. SQUID, we control a quantum phase shift by using the rotation of the Earth, and find the classic interference pattern with periodicity determined by the ³He quantum of circulation.

Our basic interferometer topology is shown in Fig. 1a. Schematically, the device is a circular loop of radius R which includes two superfluid ³He Josephson weak links^{7,8}. These weak links each consist of a 65×65 array of 100-nm apertures etched in a 60-nm-thick silicon nitride membrane. Similar arrays have previously been shown to be characterized by a current–phase relation given⁹ by the Josephson formula:

$$I = I_c \sin \phi \tag{1}$$

Here I is the mass current flowing through the array, ϕ is the quantum phase difference across the array, and I_c is the critical current characterizing the array.

The interferometer is predicted to behave as a single weak link with an effective critical current, I_c^* (see Methods). If the inter-